3D Tumor Shape Reconstruction from 2D Bioluminescence Images and Registration with CT Images

Junzhou Huang [1], Xiaolei Huang [1], Dimitris Metaxas [1], Debarata Banerjee [2]

[1] CBIM, DCIS, Rutgers University, NJ, USA
[2] Cancer Institute of New Jersey, UMDNJ, NJ, USA

Abstract— This paper introduces a novel and efficient algorithm for reconstructing the 3D shapes of tumors from a set of 2D bioluminescence images which are taken by the same camera but after continually rotating the animal by a small angle. The method is efficient and robust enough to be used for analyzing the repeated imaging of a same animal transplanted with gene marked cells. There are several steps in our algorithm. First, the silhouettes (or boundaries) of the animal and its interior hot spots (corresponding to tumors) are segmented in the set of bioluminescence images. Second, the images are registered according to the projection of the animal rotating axis. Third, the images are mapped onto 3D projection planes and from the viewpoint of each plane, the visual hulls of the animal and its interior tumors are reconstructed. Then, the intersection of visual hulls from all viewpoints approximates the shape of the animal and its interior tumors. In order to visualize in 3D the structure of the tumor, we also co-register the BLI-reconstructed crude structure with detailed anatomical structure extracted from high-resolution micro-CT on a single platform. The experimental results show promising performance of our reconstruction and co-registration method.

I. INTRODUCTION

Bioluminescence imaging (BLI) is an emerging technique for sensitive and noninvasive imaging, which can be used for monitoring molecular events in intact living animals. Important applications of this imaging technique include gene therapy and cell trafficking studies. Unlike fluorescence optical imaging approaches which require an external source of light for excitation of fluorophores, BLI generates a two-dimensional (2D) view of gene expression using a CCD camera based on the internal light produced by luciferases, catalysts in a light generating reaction, through the oxidation of an enzyme-specific substrate (luciferin) [1], [2]. The increasing use of BLI as the choice of small-animal imaging modality is based on the need for repeated imaging of the same animal transplanted with gene marked cells, which is possible using BLI. Other imaging modalities such as mPET, MRI are unsuitable for repeated imaging in a laboratory setting and require sophisticated equipment or allowance for isotope decay to image repeatedly. A complementary imaging modality to BLI is the microCT imaging, which can be used in one session to provide

the high-resolution anatomical images. The problem we tackle in this paper is to recover 3D tumor shape from multiple 2D bioluminescence images of a small animal. There is a need for 3D reconstruction because 2D BLI images do not provide any information on the response in the z-axis(i.e. depth). Recently there has been research work on bioluminescence tomography (BLT) which aims to extract the depth information [3], [4], [5]. However, as shown in [5], this inverse reconstruction problem is ill-posed and in the general case the BLT does not have a unique solution. Furthermore, real systems that implement BLT can be time consuming and not easy to reconstruct the 3D images with high resolution. One potential approach suggested in [4] is to use multiple CCD cameras for simultaneous measurement of bioluminescence signals.

In this paper, we propose a novel and efficient approach to reconstruct 3D tumor shape in small animals using a series of BLI images taken by the same camera but after continually rotating the animal by a small angle. Our image-based reconstruction technique is rooted in the stereoscopy algorithm in computer vision [6]. Instead of using multiple cameras, our experimental set-up uses a single CCD camera that is readily available in commercial BLI imaging systems (e.g. IVIS 200 imaging station) to acquire images of an animal at every rotation stage for multiple rotations clockwise from a fixed (e.g. the vertical) axis. The rotation angle is small between consecutive acquisitions to ensure the possibilities of obtaining good reconstruction results. This set-up is simpler and more flexible than using multiple cameras since we can acquire any number of images by adjusting the rotation angle.

Given the multiple BLI images of the animal, we propose to reconstruct the 3D shape of the hot spots (corresponding to tumors) based on a 3D visual hull reconstruction method. Using visual hulls for object shape reconstruction has received extensive attention and has been widely studied over the last decade [7], [8]. A visual hull is the approximation to the shape of an 3D object, and it can be computed from simple silhouettes by extending the silhouettes along the depth direction. The visual hull of an object depends both on the object itself and on the viewing direction, and an exact surface could be constructed if there are sufficient number of viewing directions. Because it is simple and efficient, visual

hull is successfully used for many virtual reality application [9]. Visual hull is well-known that it has no concavity. For solving this problem, Brand et al. [8] recently developed a method. They generalized the problem with a differential geometric setting in the dual space, in which the specified priors are not needed for fitting the parameter functions. Although the visual hull can not represent concavity, it is able to give a good estimation if the objects is textureless or has non-Lambertian effects. In this paper, since the tumors have small sizes and they are textureless in the captured images, a visual hull based 3D reconstruction method is suitable to recover the tumor shapes from multiple BLI images. In this paper, we use visual hulls to reconstruct the shape of tumors captured by a set of BLI images. The proposed method has several steps. First, the silhouettes of objects (e.g. a small animal, or a tumor inside the animal) in all the images are obtained with a simple segmentation approach. Then all the images are registered according to the rotating axis. Finally, the images are mapped onto their respective 3D projection planes, visual hulls generated from all projection directions are generated, and the intersection of all visual hulls are computed to approximate the 3D location and shape of the animal and its interior tumors. Our results on both phantom study and small animals show very good reconstruction accuracy.

Based on our work described in [10], in this paper, we combined the 3D tumor reconstructed results from BLI images and microCT images together to obtain the final visualizations. Registering and visualizing the reconstructed tumor structure from BLI together with detailed animal geometry extracted from microCT allows one to import multiple images on a single platform and obtain better structural and functional information. There has been extensive research on multi-modal image registration in the literature, either based on matching geometric features [11], [12] or by optimizing intensity-based energy functions [13], [14]. However, we know of no existing registration algorithms for registering the optical BLI and structural microCT. In this paper, we develop such a registration algorithm based on BLI reconstruction and structure (shape) registration. Using the registration algorithm we can locate the tumor sites relative to animal anatomical landmarks, and this knowledge will allow us to develop methods to generate MSCs with robust and improved tumor targeting capabilities in the future.

The remainder of the paper is organized as follows. In section 2, we introduce our experimental set up and data acquisition method. Section 3 presents the procedures for segmenting animal tumor silhouettes. Section 4 introduces the method for registering images. The visual hull reconstruction algorithm and experimental results using both a phantom study and real small-animal images are presented in section 5. Section 6 proposes the co-registration visualization results of BLI and microCT on a single platform. Section 7 concludes this paper with discussions.

II. SETUP AND IMAGE ACQUISITION

The bioluminescence images were acquired following injection of D-luciferin (given i.p. at 150mg/ml) and image reconstruction was carried out using manufacturer's (the IVIS 100 machine, by Xenogen, Alameda, CA) software. Images were acquired in a standard mode with 2x2 binning. In order to get specificity of the response in the z-axis, we design the following experimental set up.

For small animals such as mice, a 50 ml tube cut at both ends and the bottom can be used as a holder. The anesthetized animal fits easily in the tube and can be placed in the imaging device without any discomfort. The animal can be rotated similar to the phantom-well images and 32 rotational images can be acquired. An added advantage of the 50 ml tube is that it can be fitted with a soft foam to make the animal fit snugly in the tube, and the outside of the tube can be marked with fiduciary markers for anatomical reference. After the animal to be imaged is inserted into a cylindrical 50 ml tube, images are acquired at every rotation stage clockwise from the vertical axis. This generates a series of images including the one without any rotation. Fig.1 shows some example BLI images of a mouse with tumor in the abdomen area. The mouse is contained in a 50 ml tube cut at both ends and bottoms. The tumor regions have higher intensity values in the BLI images. The dimensions along long axis and short axis of the mouse tumor is $1.2cm$, $1.1cm$ and $1.1cm$, which is obtained by sacrificing mouse after image capturing. The intensity representation denotes the level of response in different locations. The bright reflections due to the tube surface are eliminated using a pre-processing filtering step before applying our reconstruction algorithm.

Fig. 1 shows some example images, between which there are small rotations. The intensity representation denotes the level of response in different locations. Due to the characteristic of the bioluminescence images, higher intensity denotes the possible location of a tumor. The bright reflections due to the tube surface are eliminated using a pre-processing filtering step before applying our reconstruction algorithm. In the following sections, we also use a set of images from a phantom study (Fig.2(1)). The images were generated by rotating a 50 ml tube clockwise at an increment of 11.25 degrees. Luciferase-positive cell lysates were embedded in agarose inside the tube. The dimensions along long axis and short axis of the cluster of lysates are $1.8cm$, $1.2cm$ and $1.1cm$. It appeared as a hot point in images which were acquired over 20 minutes following injection of D-luciferin.

Using this set up, we can easily separate the interested objects from the background. Then, with the proposed 3D reconstruction method and the segmented silhouettes, we could efficiently reconstruct the 3D shape of the tumors. We can
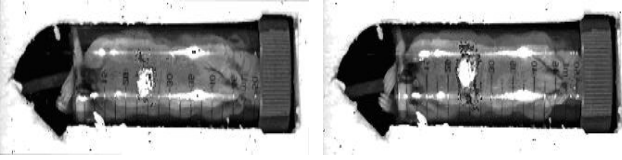
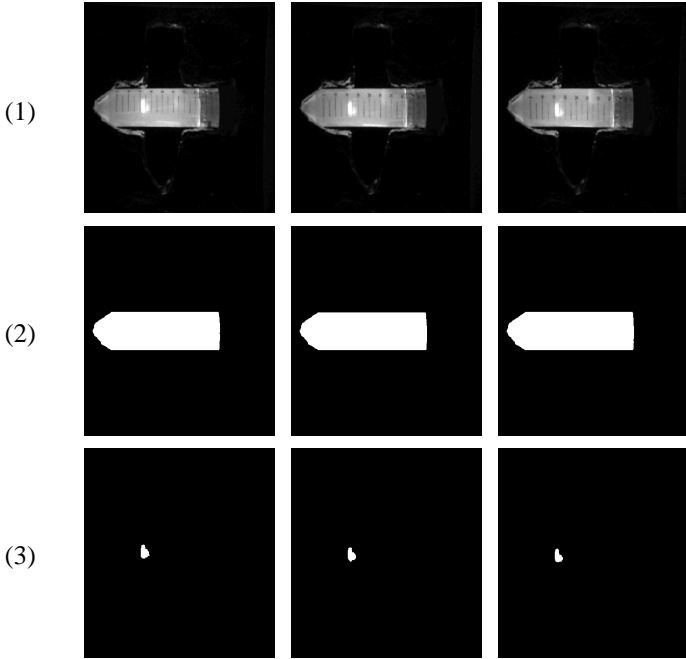Fig. 1. Examples of BLI images acquired from a small animal with tumor cells growing in the abdomen.

Fig. 2. Segmentation Examples. (1) BLI images. (2) Segmented tubes. (3) Segmented tumors

Fig. 3. Examples for registering images. (1) BLI images. (2) after alignment.

also further extend the method to register the center of mass of several more areas near the maximum response, where the intensity is 5-10% lower from this maximum. The 3D reconstruction of these points will give an estimate of the tumor enclosing volume.

III. SEGMENTING IMAGES

A visual hull depends both on the object silhouettes and on the camera viewing direction. Before the reconstruction, we should obtain the object silhouettes in the images. In our experiment, as shown in Fig. 2(1), the objects were rotated gradually with a small angle and their bioluminescence images were captured correspondingly. Considering that the images include not only the interested objects (the tube and the tumor), but also the un-interested background, the captured BLI images should be segmented for later processing. In order to facilitate correct segmentation, a monochromatic background was captured to distinguish the tube containing the small animal from the environment in the experiment setup. First, the contour (or silhouette) of the tube containing the small
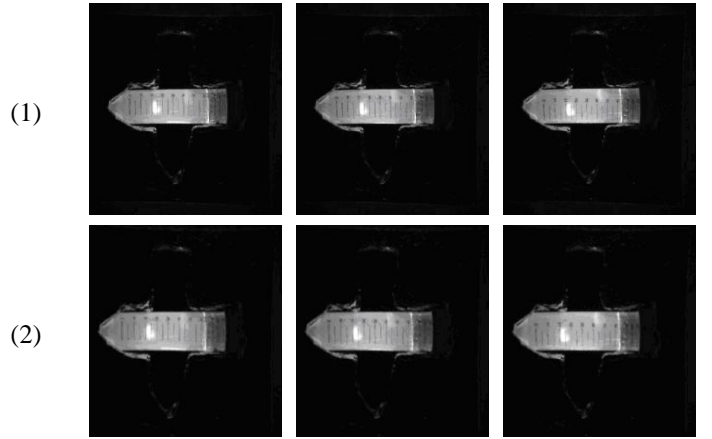
animal is easily extracted from the input images by simple thresholding. Fig. 2(2) shows the tube segmentation result we obtained. In order to segment the tumor from the tube region, the bright reflections due to the tube surface are eliminated using a pre-processing filtering step. Then, according to the characteristic of tumor in the BLI images (they appear as higher intensities), we can segment the tumor from the tube region by combining tumor intensity and edge information. Fig. 2(3) shows segmentation results of the tumor in the images.

IV. REGISTERING 2D BLI IMAGES

Due to noise in the imaging system during the rotation of the small animal, the bioluminescence images may not be perfectly aligned. To ensure accurate correspondence across images, we apply an image-based method to register the images such that projections of the rotating axis on all images overlap in the image space. For this purpose, we define an image dissimilarity objective function based on mutual information [14], [15], and recover the translation and rotation parameters by minimizing the objective function. Suppose a source image is f, and its adjacent target image is g.

In the most general case, let us consider a sample domain Ω in the image domain of the source image f, we aim to recover the parameters $\Theta = (T_x, T_y, \theta)$ of a global transformation A such that the mutual information between $f_\Omega = f(\Omega)$ and $g_\Omega^A = g\big(A(\Theta; \Omega)\big)$ is maximized. Here the parameters T_x and T_y are translation parameters in the x and y directions respectively, and θ denotes the rotation angle. And the definition for such mutual information is:

$$MI(X^{f_\Omega}, X^{g_\Omega^A}) = \mathcal{H}\left[X^{f_\Omega}\right] + \mathcal{H}\left[X^{g_\Omega^A}\right] - \mathcal{H}\left[X^{f_\Omega, g_\Omega^A}\right] \quad (1)$$

In the above formula, X denotes the intensity random variable and $\mathcal{H}$ represents the differential entropy. Then we define the image dissimilarity objective function as:

$$E(A(\boldsymbol{\Theta})) = -MI(X^{f_\Omega}, X^{g_\Omega^A}) \qquad (2)$$

Hence by minimizing this objective function E, we achieve maximizing mutual information. The calculus of variations with a gradient descent method is then used to minimize E and recover the transformation parameters T_x, T_y and θ. Fig. 3(2) shows the registered images. Note that small displacements and rotations between consecutive images are corrected.

V. RECONSTRUCTING 3D STRUCTURE AND TUMOR SHAPE

As introduced above, instead of setting up an image-capturing system with multiple cameras, we take biolumi-nescence pictures by a single fixed camera while rotating the object (tube or small animal). This setup is equivalent to having multiple cameras surrounding a static object, but it is much simpler and does not require calibrating multiple cameras. Fig. 5 demonstrates the multi-view set up where the planes represent the projection planes for images taken from different views. Since the depth variation due to the object is small compared with the distance between the animal and the camera, changes in the object silhouette along the depth direction are negligible. Thus, an orthographic projection model is reasonable to use in order to reconstruct the 3D object structure and tumor shape.

After all images are aligned so that the projections of the rotating axes overlap, we compute feature correspondences between consecutive images in order to reconstruct the 3D locations of those features. This is achieved by detecting corner features on both images, and establishing correspon-dences based on maximizing mutual information between small-neighborhood regions around the features.

To detect corner features on an image I, we consider the spatial image gradient (i.e. first order derivatives), $[I_x, I_y]$. For a neighborhood Q surrounding a pixel p, we form the matrix $\mathbf{C}$, defined as:

$$\mathbf{C} = \left(\begin{array}{cc} \sum I_x^2 & \sum I_x I_y \\ \sum I_x I_y & \sum I_y^2 \end{array} \right)$$

where the sums are taken over the neighborhood Q. Then we apply principal component analysis to compute the two eigenvalues λ_1 and λ_2 ($\lambda_1 \geq \lambda_2$) of the matrix $\mathbf{C}$, and choose corner features as those neighborhoods with $\lambda_1 \geq \lambda_2 > 0$ and the smaller eigenvalue λ_2 is larger than a threshold.

To measure the similarity between small-neighborhood re-gions around corresponding feature points on two consec-utive images, we use the multi-modal similarity measure, Mutual Information, because nonlinear changes exist in feature appearance due to planar projection after rotation. Fig. 4 shows examples of correspondences established between two consecutive images (corresponding points are marked by the same number).
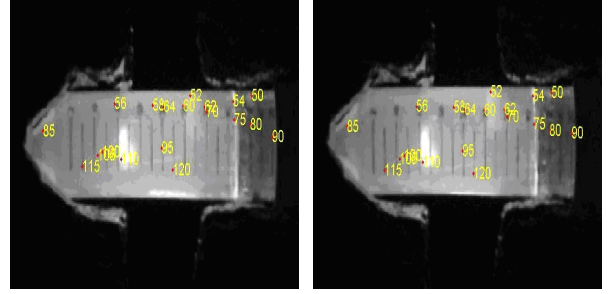

Fig. 4. Feature correspondences established between two consecutive images.

Our 3D tumor shape reconstruction is based on the concept of visual hull. As introduced in [7], [9], [16], a visual hull is defined by a set of camera locations, the internal calibration parameters of the camera and silhouettes from each view. It can be simply thought as the maximal volume that creates all possible silhouettes of an object. It is obvious that the visual hull should include the object and be included in the convex hull of the object. Generally, the visual hull is usually computed with small number of silhouettes. Matusik and his colleagues introduced an efficient technique for generating the visual hull in his work. His approach computes the intersection of the viewing ray from each designated viewpoint with each pixel in the image of that viewpoint [9]. Then, visual hull based reconstruction methods have the advantage that they can be performed quickly. At the same time, they are also much less expensive in terms of storage requirements than volumetric approaches such as voxel carving [17]. Moreover, if we can obtain accurate estimation of each image views and the internal calibration parameters of the camera, a relatively small number of views (4-8) is often sufficient to recover the 3D object shape for these techniques. Thus, it is very useful and popular for creating real-time virtual models of objects in practice.

Formally, the visual hull of an object S with respect to the viewing region R, denoted by $VH(S, R)$, is a volume in space such that for each point P in $VH(S, R)$ and each viewpoint V in R, the half-line from V through P contains at least one point of S [7]. This definition simply states that the visual hull consists of all points in space whose images lie within all silhouettes viewed from the viewing region. Stated another way, the visual hull is the maximal object that has the same silhouettes as the original object, as viewed from the viewing region. It is useful to think of an alternative, constructive definition of the visual hull with respect to a viewing region. Given a point V in the viewing region R, the silhouette of the object as seen from V defines a generalized cone in space with its apex at V map images taken from different views onto their respective projection planes. Similar to the basic idea in all the visual-hull reconstruction algorithms [7], [9], [16], in our implementation, due to using the orthographic projection model, the segmented object and
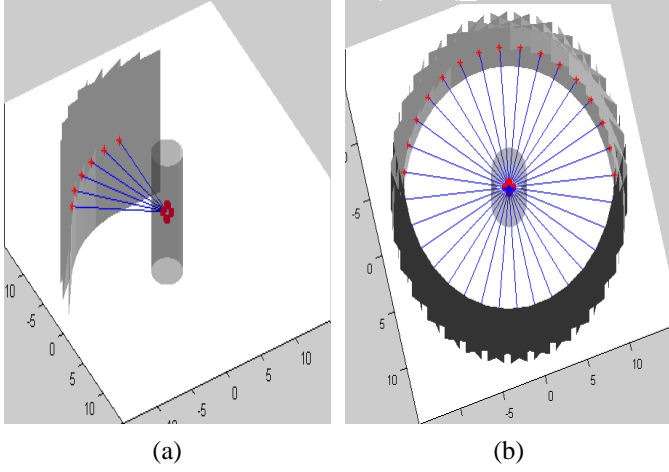
Fig. 5. Setting up projection plane geometry for images taken from different views. (a) some example views for consecutive images. (b) all views forming a full circle.

tumor silhouettes are projected into the 3D space by cylindrical visual hulls, instead of conical visual hulls in the projective projection model. By computing the intersection of the visual hulls projected from all images (i.e. all viewing directions), we obtain the estimation for the shape and location of the animal and its interior tumors.

A. Experimental Results

First, we perform several phantom studies. Fig. 6(a) demonstrates the process of determining the 3D depth of feature points by computing the intersection of 3D rays passing perpendicularly through corresponding feature points on two consecutive images, which are mapped onto their respective projection planes. It shows the reconstructed 3D location of the tube center (the intersection of the two rays in blue) and the 3D location of the tumor center (the intersection of the two rays in red). The tumor centers on the bioluminescence images are computed as the centroids of the high-intensity signal regions (drawn as asterisks on the image planes), and the intersection of 3D rays passing through tumor center locations on images taken from different views gives us the location of the tumor center in 3D. Fig. 6(b) shows the intersection of multiple cylindrical hulls based on the tumor silhouettes. The intersection of all cylindrical hulls gives the 3D reconstruction of the tumor shape. When we compute the visual hull of the tumor, we can obtain the 3D tumor structure. In the phantom study, since the object surface can be approximated using a cylinder, we determine the radius of the cylinder using silhouettes of the tube. Fig. 7 shows the reconstructed 3D tumor viewed in two directions. Fig. 8 shows the reconstructed shape of the tube and tumor, which are viewed in two different directions.

We also do the same procedures to reconstruct animal and tumor shapes from small-animal BLI images. Fig. 11(a-b)

shows the reconstructed tumor location and shape from a set of BLI images of the mouse with abdominal tumor.

Based on our approach, we establish the relationship between the reconstructed animal dimension measurements in the animal centered reference frame and that in the physical world. This is achieved by computing the conversion ratio based on one base measurement, such as the diameter or the length of the tube or mouse).
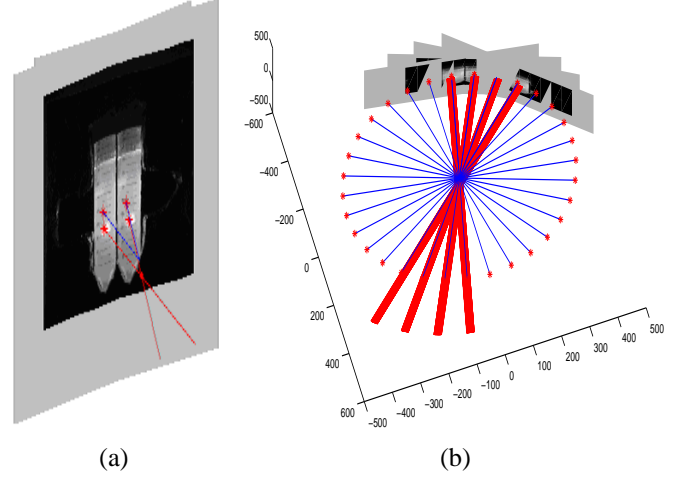

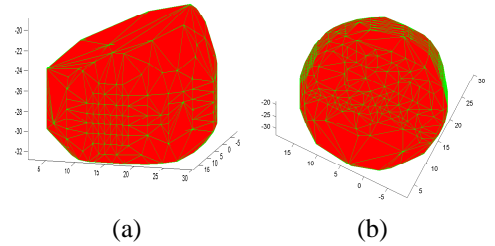Fig. 6. Examples for visual effect (a) Line intersection. (b) Cylinder hull intersection.

Fig. 7. Reconstructed 3D tumor shape from two views.

B. Evaluation

Evaluation of the reconstruction accuracy is done by comparing the recovered 3D shape and location of the tumor with the ground truth in our experimental set up.

In our phantom study example, validation of the reconstruction accuracy is done by comparing the recovered 3D shape and location of the tumor with the ground truth in our experimental set up. Visually from Fig. 8, we can see that the estimated tumor location is within the tube and has a reasonable 3D shape. At the same time, we also measured physically the tumor center location, and dimensions along the long axis and short axis of the cluster of luciferase-positive cell lysates that appeared as hot (or bright) spots in the images. Comparing our reconstruction result with the
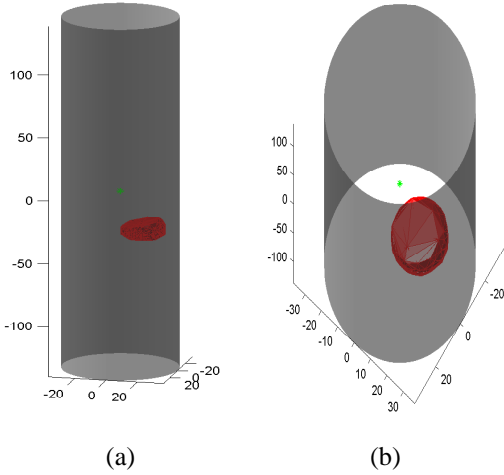
Fig. 8. Reconstructed 3D tumor (red) in the tube (gray) in the phantom study, from two views
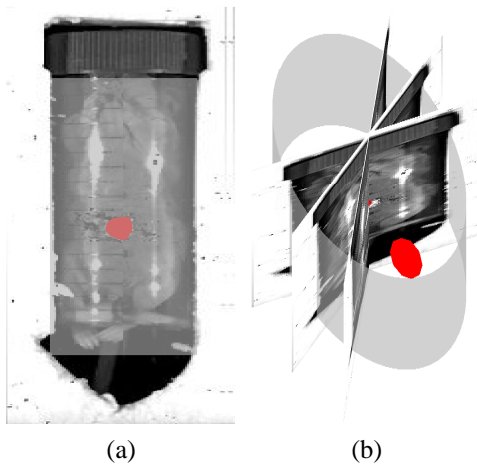

Fig. 9. Reconstructed 3D tumor (red) in the tube (gray) containing the mouse, from two views.

ground truth (Detailed in section II), the distance in 3D between the measured hot spot center and the reconstructed center is around $2mm$, the difference between the long axis dimensions is less than $1mm$, and the difference between the short axis dimensions is less than $1mm$. For the mouse example, the reconstructed tumor dimensions are all less than $2mm$ different from the true dimensions, and the reconstructed tumor location matches with the ground truth acquired by sacrificing the mouse.

VI. REGISTRATION WITH MICRO-CT ON SMALL ANIMALS

Using the algorithm described above, we can recover the tumor shapes in animals. One key difference is that, because the geometry of an animal is much more complicated than a tube, it is difficult to reconstruct the 3D animal surface satisfactorily using the sparse surface points recovered. Our solution is to co-register the crude structure reconstructed from

bioluminescence images with structural microCT tomographic images. This co-registration of BLI and microCT on a single platform has the advantage of combining the strengths of BLI which are: low cost and repetitive imaging, and that of microCT which are: high-resolution and containing detailed structural information.

In preparation for the BLI/microCT images, an animal was injected through tail vein with 2×10^4 tumor cells expressing luciferase. Tumors were formed in the abdomen and could be imaged by BLI(on day 12 after injection) following injection of 150mg/kg D-luciferin given intraperitoneally. The animal was anesthetized with isolflurane inhalation, injected with 150mg/kg D-luciferin and immobilized in an open 50 ml tube and placed on the imaging stage of the IVIS 100 machine (Xenogen, Alameda, CA). Images were acquired for two rotations on each side of the fixed central axis at 11.25 degrees. Examples of BLI images acquired can be seen in Fig. 1. The same animal was carried over to the microCT machine in the same position while remaining under isoflurane anesthesia. MicroCT images (512 slices) were acquired on an IMTEK microCT machine. Examples of microCT slices for the same animal are shown in Fig. 10.
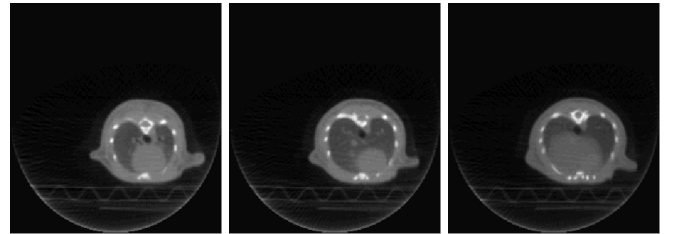

Fig. 10. Examples of microCT images from the same animal as in Fig. 1.

We followed similar procedures to that in the phantom study for reconstruction using BLI images. First, the BLI images are registered by aligning the projections of the rotating axes. Then both 3D mouse surface points and 3D tumor center locations are recovered in the virtual rotating camera set up using the set of bioluminescence images. Fig. 11(a-b) shows the reconstructed 3D tumor location and shape. In our experiments, the living mouse is undergoing repetitive imaging, which allows us to obtain temporal information.

On the other hand, the mouse is imaged once in the beginning of the study. We extract the mouse surface and skeleton structures using standard segmentation and visualization techniques. We use both landmark feature information and the Iterative Closest Point (ICP) technique [18] to register the crude 3D structure reconstructed from BLI images with the detailed 3D structure reconstructed from microCT.

The Iterative Closest Point Algorithm [18] is widely used for registering two partially overlapping but slightly misaligned images. It has proven to be very useful registration method in the processing of 3D image data. The key idea of ICP is described as follows: Given two surfaces S and S', in order to
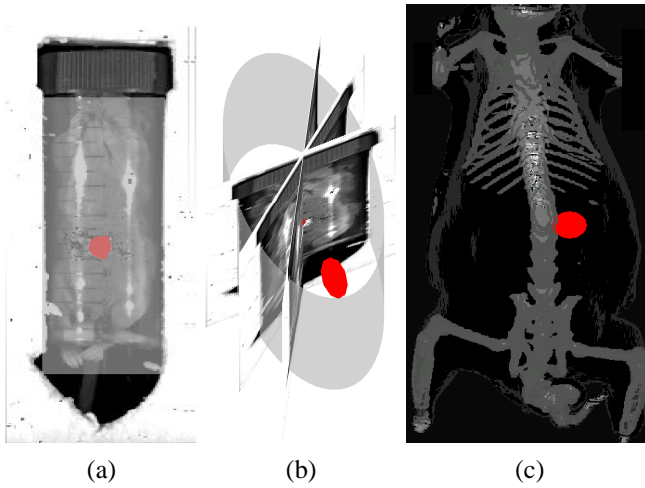
Fig. 11. (a) Frontal view of reconstructed tumor location superimposed on a projected image. (b) another view of the reconstructed tumor location, showing relative position with respect to three projected images. (c) reconstructed tumor superimposed on the detailed mouse geometry from microCT.

register these two surfaces, we can search a deformation. After this deformation, point P in surface S should be "close" to its corresponding point P' in surface S'. In order to measure the metric of "close", one function is introduced as follows:

$$Func = \sum_i dist^2(F(P_i) - P_j) \qquad (3)$$

If this function has a small values, it means that two points P_i and P_j are "close". Generally, ICP includes two main steps: 1) Given a deformation $F : Mp = F(P)$ with known parameters, we can apply this deformation to the surface S to get a model surface Ms. Suppose P is the point in the surface S. For every point Mp in Ms, find its closest point P' in the surface S'. P'_j is the corresponding point that has been found in this iteration for point P; 2) Now, we can compute the function defined in equation 3. In this time, P and P' are known but the parameters of deformation F is unknown. Minimize the function value to get new deformation parameters. We can repeat these two steps until the termination criterion is reached.

After the registration with ICP, we are able to visualize the recovered 3D tumor location and shape from BLI together with the detailed geometry from microCT. Fig. 11(c) shows the final registration and tumor shape result in 3D.

VII. DISCUSSIONS AND CONCLUSIONS

We have presented a novel image-based framework for 3D tumor shape reconstruction from a series of 2D biolumines-cence images and for registering reconstructed BLI structure with animal geometry extracted from high resolution micro-CT images. This is the first image-based BLI reconstruction method presented, to the best of our knowledge, and the simplicity and efficiency of our framework gives it great potential in studying cell trafficking, tumor growth, response to therapy in vivo as well as imaging and analyzing processes such as hematological reconstitution following bone marrow transplantation, among others. Experimental results on both phantom data and small animal data show that the proposed method has encouraging performance for 3D tumor shape reconstruction from 2D Bioluminescence Images and co-registration with CT Images.

REFERENCES

[1] P. Mayer-Kuckuk, L. G. Menon, R. G. Blasberg, J. R. Bertino, and D. Banerjee, "Role of reporter gene imaging in molecular and cellular biology," *Journal of Biological Chemistry*, vol. 385, pp. 353–361, 2004.

[2] B. Iris, Y. Zilberman, E. Zeira, E. Galun, A. Honigman, G. Turgeman, T. Clemens, Gazit Z., and Gazit D., "Molecular imaging of the skeleton: quantitative real-time bioluminesence monitoring gene expression in bone repair and development," *Journal of bone and mineral research*, vol. 18, pp. 570–578, 2003.

[3] X. Gu, Q. Zhang, L. Larcom, and H. Jiang, "Three-dimensional bioluminescence tomography with model-based reconstruction," *Optics Express*, vol. 12, no. 17, pp. 3996–4000, 2004.

[4] G. Wang, E. A. Hoffman, G. McLennan, L.V. Wang, M. Suter, J. F. Meinel, and et al., "Development of the first bioluminescent ct scanner," *Radiology*, vol. 229, no. P, pp. 566, 2003.

[5] G. Wang, Y. Li, and M. Jiang, "Uniqueness theorems in bioluminescence tomography," *Medical physics*, vol. 31, pp. 2289–2299, 2004.

[6] N. Ayache, *Artificial Vision for Mobile Robots: Stereo vision and Multisensory Perception*, MIT Press, Cambridge (MA), 1991.

[7] A. Laurentini, "The visual hull concept for silhouette-based image understanding," *IEEE Transactions on Pattern Analysis and Machine Intelligence*, vol. 16, no. 2, pp. 150–162, February 1994.

[8] M. Brand, K. Kang, and D. Cooper, "Algebraic solution for the visual hull," in *IEEE Conference on Computer Vision and Pattern Recognition*, 2004, vol. 1, pp. 30–35.

[9] W. Matusik, C. Buehler, L. McMillan, and S Gortler, "Image-based visual hulls," in *SIGGRAPH2000*, 2000, pp. 187–194.

[10] J. Huang, X. Huang, D. Metaxas, and D. Banerjee, "3d tumor shape reconstruction from 2d bioluminescence images," in *IEEE Int'l Symposium on Biomedical Imaging: From Nano to Macro*, 2006, pp. 606–609.

[11] J. Thirion, "New feature points based on geometric invariants for 3D image registration," *International Journal of Computer Vision*, vol. 18, no. 2, pp. 121–137, May 1996.

[12] A. Can, C.V. Stewart, B. Roysam, and H.L. Tanenbaum, "A feature-based, robust, hierarchical algorithm for registering pairs of images of the curved human retina," *IEEE Transactions on Pattern Analysis and Machine Intelligence*, vol. 24, no. 3, pp. 347–364, 2002.

[13] A. Collignon, F. Maes, D. Vandermeulen, P. Suetens, and G. Marchal, "Automated multimodality image registration using information theory," in *Proc. of Information Processing in Medical Imaging*, 1995, pp. 263–274.

[14] P. Viola and W. Wells, "Aligment by Maximization of Mutual Informa-tion," in *IEEE International Conference of Computer Vision*, 1995, pp. 16–23.

[15] F. Maes, A. Collignon, D. Vandermeulen, G. Marchal, and P. Suetens, "Multi-modality image registration by maximization of mutual infor-mation," *IEEE Transactions on Medical Imaging*, vol. 16, no. 2, pp. 187–198, 1997.

[16] K. Grauman, G. Shakhnarovich, and T. Darrell, "A bayesian approach to image-based visual hull reconstruction," in *IEEE Conference on Computer Vision and Pattern Recognition*, 2003, vol. 1, pp. 187–194.

[17] K. Kutulakos and S. Seitz, "A theory of shape by space carving," *International Journal of Computer Vision*, vol. 1, no. 3, pp. 307–314, March 2000.

[18] Z. Zhang, "Iterative point matching for registration of free-form curves and surfaces," *International Journal of Computer Vision*, vol. 13, no. 2, pp. 119–152, 1994.